Field Modeling for Plate-Core Inductor With Significant Fringing Using Equal-Flux Contours

Han Cui[1], Joyce Mullenix[2], Roberto Massolini[2], and Khai D. T. Ngo[1], *Fellow, IEEE*

[1]Center for Power Electronics Systems, Virginia Polytechnic Institute and State University, Blacksburg, VA 24061 USA
[2]Texas Instruments Incorporated, Dallas, TX 75243 USA

An inductor with winding sandwiched between two core plates is analyzed to model the nonuniform distribution of magnetic field. The winding is placed near the edge of the core to maximize the energy within the limited footprint such that the amount of energy stored outside the core volume is not negligible. The proportional-reluctance, equal-flux model is developed to build the contours with equal amount of flux by governing the reluctance of the flux path. The shapes of the flux lines are modeled by different functions that are guided by the finite-element simulation. The field calculated from the flux lines enables calculation of inductance, winding loss, and core loss. The inductance is used as a figure of merit to evaluate the modeling accuracy. Prototypes made of flexible circuit for inductors with different layouts are measured to verify the model. The measured inductances agree with the modeled result by less than 13% error.

***Index Terms*—Flux contours, magnetic field modeling, planar magnetics, plate core.**

I. Introduction

PLANAR magnetics [1]–[8] are widely used in high-frequency power converters for the benefits of low profile and capability for integration. Research on miniature power converters using planar cores and printed circuit board winding technologies [3]–[9] shows significant improvements in power density and thermal characteristics compared to conventional wire-wound magnetic components. Analytical models of the planar magnetics are useful for designing and optimizing the performance [10]–[15], among which modeling the magnetic field is essential since all the performance factors (inductance, winding loss, core loss, and so on) depend on the field distribution.

A. Plate-Core Inductor

The plate-core structure discussed herein is simple and easy for manufacturing, because the core has no vertical bridges such as the E-cores and PQ cores. The plate-core inductor comprises a spiral winding sandwiched between top and bottom magnetic plates as shown in Fig. 1(a). This structure not only improves the inductance by more than three times compared to the air-core inductor [11]–[14] but also has the potential advantage of being compatible for integrated circuits [1], [3].

There are several existing methods for modeling the field of the plate-core inductor. A classical way is using the current image method [14] by reflecting the current between the boundaries alternately and using these image currents to calculate the magnetic potential A. Another method is based on the mutual inductance calculation for two filaments given by Maxwell with the additional impacts from the core plates [15]. Both methods work well when the core plates

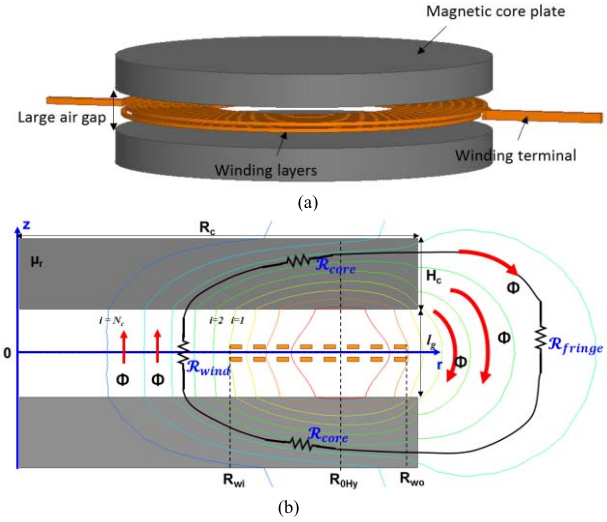

Fig. 1. (a) Plate-core inductor. (b) 2-D cross-section view in cylindrical coordinates showing equal-flux contours and constituent reluctances of one path.

radius R_c can be considered infinitely large compared with the winding outer radius (e.g., $R_c > 2R_{\mathrm{wo}}$). However, the boundary conditions become extremely complex and require large amount of computation effort when the winding is similar in dimension to the core plates (e.g., $R_c \approx R_{\mathrm{wo}}$). Applying these existing methods to the finite plate-core structure results in more than 35% error as shown in Fig. 2. The transmission line model used in [16] and [17] tried to solve the flux distribution in micro transformers with thin-film structures where the magnetic flux inside the core plate only has the lateral direction, which may oversimplify the field calculation when a certain core thickness is required to achieve the inductance value.

Compared to the conventional structure discussed in existing literatures, the plate-core structure studied herein has the following characteristics:

1) The winding is placed near the core radius R_c for the benefit of higher inductance within a given footprint

Manuscript received January 16, 2017; revised April 13, 2017; accepted May 27, 2017. Date of publication June 2, 2017; date of current version August 17, 2017. Corresponding author: H. Cui (e-mail: hancui@vt.edu).

Color versions of one or more of the figures in this paper are available online at http://ieeexplore.ieee.org.

Digital Object Identifier 10.1109/TMAG.2017.2710948

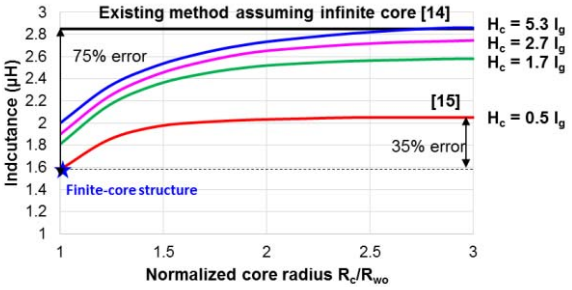

Fig. 2. Comparison of error in inductance by applying [14] and [15] to plate-core inductors with finite core dimension ($R_{\text{wo}} \approx R_c$).

area for those applications insensitive to electromagnetic interference caused by stray field. It is studied from the finite-element simulation (FES) that larger winding radii (R_{wi} and R_{wo}) increase the inductance density, and the quality factor reaches the peak when the winding outer radius R_{wo} is close to the R_c. Modeling the boundary conditions and the fringing behavior are the primary challenges to calculate the field distribution accurately [18].

2) The magnetic material should have a relative permeability at least more than 5 to comply with the approximation of flux shape in the modeling methodology. This paper takes into account the field distribution inside the core as one important factor. When the permeability is too small, the flux is hardly constrained by the core plates and the flux distribution is similar to that of an air-core inductor discussed in [14] and [15].
3) When the air gap is extremely large, there is barely any flux travels from one plate to the other and the leakage flux becomes too large. The inductance is mainly controlled by the air gap length, and the contribution from the core plates becomes trivial. Therefore, the method herein is valid for those structures with $R_c/l_g > 5$ where the flux in the core and fringing area preserves elliptical and circular patterns, respectively.

B. Methodology

The plate-core structure is divided into winding, core, and fringing regions. The winding region is the gap between the two core plates, i.e., $|z| < Z_p$ and $0 \le r \le R_c$, where $Z_p = 0.5l_g$ is the vertical coordinate of the bottom surface of the top core plate. The core region comprises the core plates, i.e., $Z_p \le |z| \le Z_p + H_c$ and $0 \le r \le R_c$. The fringing region is covered by $|z| > Z_p + H_c$ or $r > R_c$.

The magnetic flux density $\boldsymbol{B}$ is found from the magnetic vector potential $\boldsymbol{A}$ by $\boldsymbol{B} = \nabla \times \boldsymbol{A}$. Under axisymmetric assumption, $\boldsymbol{A} = A_\varphi \cdot \hat{\boldsymbol{\varphi}}$ and [1]

$$\boldsymbol{B} = \nabla \times \boldsymbol{A} = \frac{1}{r}\left(-\frac{\partial(rA_\varphi)}{\partial z}\hat{\boldsymbol{r}} + \frac{\partial(rA_\varphi)}{\partial r}\hat{\boldsymbol{z}}\right). \tag{1}$$

Note that rA_φ has dimension of flux and unit of Webers. A contour/surface of equal rA_φ is thus called an "equal-flux contour/surface" herein.

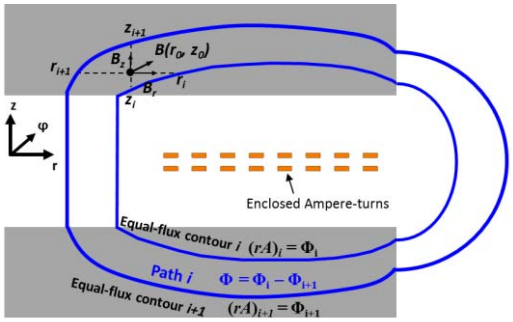

Fig. 3. Flux density of an arbitrary point sandwiched by two equal-flux contours.

Equal-flux contours Φ_i and Φ_{i+1} are exemplified in Fig. 3, where $1 \le i \le N_c$, N_c is the number of contours. The area between these contours defines "path" i. The magnetic flux density B at the point (r_0, z_0) within path i is approximated by the discretized version of (1)

$$\boldsymbol{B}(r_0, z_0) = \frac{1}{r_0}\left(-\frac{\Phi_i - \Phi_{i+1}}{z_i - z_{i+1}}\hat{\boldsymbol{r}} + \frac{\Phi_i - \Phi_{i+1}}{r_i - r_{i+1}}\hat{\boldsymbol{z}}\right) = B_r\hat{\boldsymbol{r}} + B_z\hat{\boldsymbol{z}}. \tag{2}$$

Finding $\boldsymbol{B}$ is thus synonymous to identifying the functions for the equal-flux contours.

For simplicity, $\Phi_i - \Phi_{i+1}$ is set to a constant Φ herein. This "constant Φ" is captured by the words "equal-flux" in proportional-reluctance, equal-flux (PREF). An example of equal-flux contours enclosing constant-Φ paths generated by FESis shown in Fig. 1(b).

Each path i encloses Ampere-turns $N_i I$. It is characterized by a reluctance $\Re_{\text{path\_}i}$ [18], [19]. The contours Φ_i are synthesized such that

$$\Re_{\text{path\_}i} = \frac{N_i I}{\Phi} \quad \text{or} \quad \Phi = \frac{N_i I}{\Re_{\text{path\_}i}}. \tag{3}$$

The proportionality between $\Re_{\text{path\_}i}$ and $N_i I$ in (3) is captured by the words "proportional-reluctance" in PREF.

The objective of the PREF model is to construct the equal-flux contours for magnetic field calculation. The synthesis procedure is seeded by generating contours Φ_1 and Φ_2 by the procedure described in Section II. The reluctance $\Re_{\text{path\_1}}$ is calculated for path 1 (formed by contours Φ_1 and Φ_2) by the equations in Section III. The value for Φ is obtained from $\Phi = NI/\Re_{\text{path\_1}}$ where NI is the total Ampere-turns. The reluctances $\Re_{\text{path\_}i} (2 \le i \le N_c - 1)$ are calculated from (3), and contours $\Phi_i (3 \le i \le N_c)$ are synthesized by the procedure in Section IV. The distribution of $\boldsymbol{B}$ throughout the volume is determined from (2) and validated by FES in Section V. The energy and inductance are then calculated and verified experimentally in Section VI. Conclusions and future works are given in Section VII.

II. Functions for the Flux Lines

Each equal-flux contour Φ_i is uniquely specified by its intersections with the core edges at $(R_{x(i)}, \pm Z_p)$ as shown in Fig. 4. It is modeled by piecewise continuous functions as it

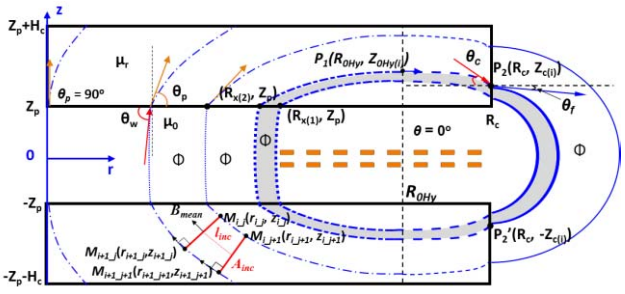

Fig. 4. Shape of flux lines at the cross-sectional area and initialized path for calculation of total reluctance $R_{\text{path\_1}}$ and magnetic flux Φ shown in Fig. 1.

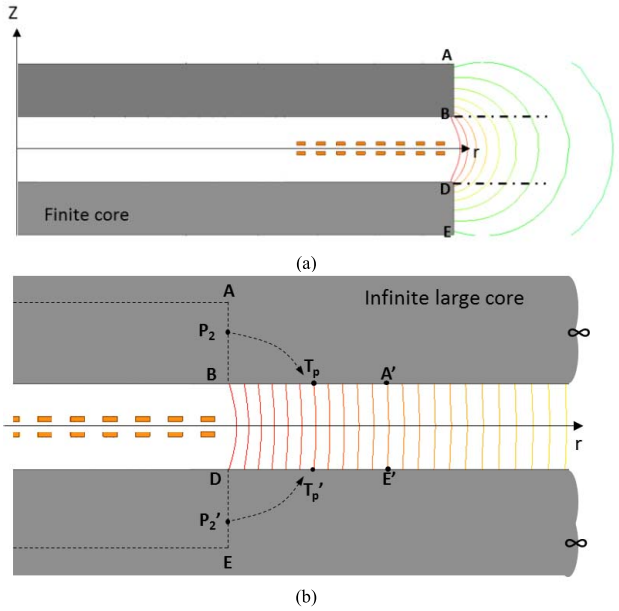

Fig. 5. (a) Plate-core inductor with fringing flux lines in the physical domain. (b) Structure in the strip domain with infinite large core and straight flux lines.

traverses the winding, core, and fringing regions. An elliptical function with two unknowns and a hyperbolic tangent function with three unknowns describe the contour in the core region. A second elliptical function with two unknowns describes the contour in the winding region. The Schwarz–Christoffel (SC) transformation [20]–[22] is used to generate the contours in the fringing region. It is discussed first in Section II-A as it involves no unknowns. Sections II-B and II-C explain how to solve the unknowns for the functions from the boundary conditions and the specified point $(R_{x(i)}, \pm Z_p)$.

A. Fringing Region

Fig. 5(a) suggests that the flux in the fringing area is hard to model using simple functions because of the finite dimensions of the core and the crowding effect around the corners. However, when the core becomes infinitely large, as shown in Fig. 5(b), the flux can be modeled as straight lines. MATLAB provides a toolbox that employs the SC transformation [20]–[22] to transform the structure in Fig. 5(a) and (b) based on numerical solutions. This toolbox used herein for generating the flux contours in the fringing area and the

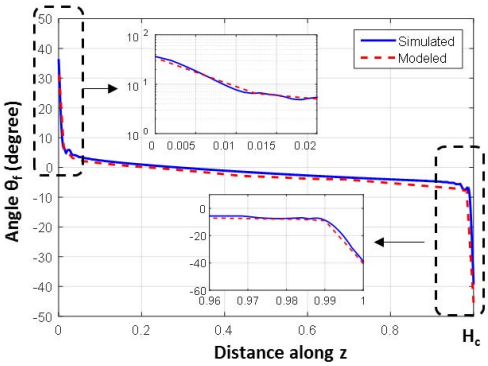

Fig. 6. Simulated and modeled θ_f in Fig. 4 for $Z_p < z < Z_p + H_c$ at $r = R_c$.

boundary angles θ_f along the right edge of the plate core. The flux contours in the fringing region are obtained by reversely mapping the straight flux lines back to the finite core structure. The boundary angles θ_f and θ_c are to be used for solving the parameters in the core region in Section II-B.

The core radius R_c, core thickness H_c, and air gap length l_g are the three inputs for the transformation, and the detailed procedure and mapping equations are given in Appendix B. Therefore, the flux line flowing from an arbitrary point $P_2(R_c + Z_c \cdot j)$ on the top core plate to the corresponding point $P_2'(R_c - Z_c \cdot j)$ on the bottom core plate [see Figs. 4 and 5(b)] can be obtained by transforming the vertical line connecting point T_p (map of P_2) to point T_p' (map of P_2').

The boundary angles θ_f along the right edge of the core plate are numerically found from the derivative of the flux lines. For example, $P_3(R_c + \Delta r_i,\ Z_c + \Delta z_i)$ is a point close to boundary point $P_2(R_c + Z_c \cdot j)$ along the ith flux line, and the boundary angle is calculated from

$$\theta_{f\_i} = \arctan \frac{\Delta z_i}{\Delta r_i}. \tag{4}$$

The plot of θ_f along core plate is shown in Fig. 6 comparing the result from SC transformation and FES. For simplicity, only the fringing contours along the right edge of the plates [*AB* and *DE* in Fig. 5(a)] are considered. Although the fringing contours starting from the upper (lower) edge of the top (bottom) plate can be constructed in the same method, the reluctances formed by these contours are 2.6% of the total reluctance and thus neglected.

The tangential angle at point $P_2(R_c, Z_{c(i)})$ is noted as θ_c as shown in Fig. 4, where θ_c along the right edge of the core plate is obtained from the boundary conditions of the contour angles θ_f in the fringing area

$$\tan \theta_c = \mu_r \tan \theta_f. \tag{5}$$

Fig. 7 compares the angles θ_c modeled from SC transformation with those simulated with different R_c normalized to l_g. The modeled angles match well with simulation when the R_c/l_g is greater than 5 with less than 5 degree difference. When the core radius R_c is comparable to the air gap length l_g, SC transformation is not valid for predicting the flux lines since the core plate cannot be assumed infinite compared to air gap.

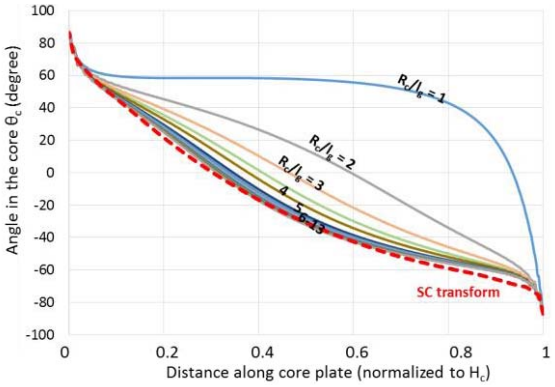

Fig. 7. Simulated θ_c in Fig. 4 with different R_c/l_g compared to modeled result from SC transformation for $Z_p < z < Z_p + H_c$ at $r = R_c$.

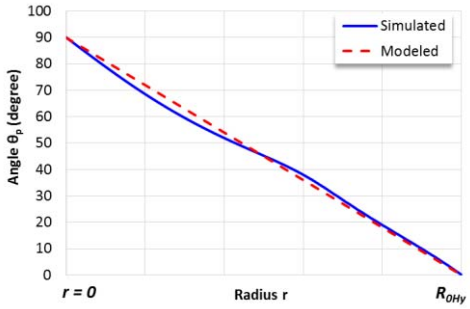

Fig. 8. Simulated and modeled θ_p in Fig. 4 versus radius with $H_c = 0.2R_c$.

B. Core Region

The objective of Section II-B is to construct the contours in the core region as shown in Fig. 1(b). The core region is divided into two subregions by the zero-flux position R_{0Hy} where the flux reverses direction and the vertical magnetic field becomes 0 (see Fig. 4). The calculation of R_{0Hy} is discussed in Appendix A. The ith flux line in the core (see Fig. 4) starts from point $(R_{x(i)}, Z_p)$, goes through middle point $(R_{0Hy}, Z_{0Hy(i)})$, and ends at point $(R_c, Z_{c(i)})$, where Z_p, R_{0Hy}, and R_c are known parameters, and $Z_{0Hy(i)}$ and $Z_{c(i)}$ are variables for each contour and they are determined from $R_{x(i)}$ specified. Section IV discusses that $R_{x(i)}$ is numerically searched for each contour such that the constant-flux requirement is satisfied. It is regarded as a known parameter in this section.

An elliptical function and a hyperbolic tangent function are used to model each contour inside the core. From $(R_{x(i)}, Z_p)$ to $(R_{0Hy}, Z_{0Hy(i)})$, elliptical functions $f_{c1\_i}(r, z)$ are used to describe the shape; from middle point $(R_{0Hy}, Z_{0Hy(i)})$ to endpoint $(R_c, Z_{c(i)})$, hyperbolic tangent functions $f_{c2\_i}(r, z)$ are used to describe the shape of the contour

$$f_{c1\_i}(r,z): \ \frac{(r - R_{0Hy})^2}{a_{\text{core\_}i}^2} + \frac{z^2}{b_{\text{core\_}i}^2} = 1 \tag{6}$$

$$f_{c2\_i}(r,z): \ z = \gamma_i \cdot \tanh(\alpha_{\text{core\_}i} \cdot (\beta_i - r)) \tag{7}$$

where $a_{\text{core\_}i}$, $b_{\text{core\_}i}$, α_i, β_i, and γ_i are the unknowns for ith contour.

All the unknowns in the two functions are solved from two boundary conditions (θ_p and θ_f) and the specified point $((R_{x(i)}, Z_p)$.

With a given value of the starting point $(R_{x(i)}, Z_p)$, the two unknowns $a_{\text{core\_}i}$ and $b_{\text{core\_}i}$ in (6) are determined from the conditions that point $(R_{x(i)}, Z_p)$ is on the ellipse and the initial angle is θ_p at point $(R_{x(i)}, Z_p)$

$$\frac{(R_{x(i)} - R_{0Hy})^2}{a_{\text{core\_}i}^2} + \frac{Z_p^2}{b_{\text{core\_}i}^2} = 1 \tag{8}$$

$$\tan\theta_p(R_{x(i)}) = \frac{-b_{\text{core\_}i}^2 (R_{x(i)} - R_{0Hy})}{a_{\text{core\_}i}^2 Z_p}. \tag{9}$$

It is approximated that the initial angle θ_p of the ellipses along the bottom core plate from 0 to R_{0Hy} decreases linearly from 90° to 0°

$$\theta_p(r) = 90^o \cdot (1 - r/R_{0Hy}). \tag{10}$$

The comparison of this approximation and the simulation result is shown in Fig. 8. This assumption is validated by simulation results under various core plate thickness ranges from *0.1* to $0.5R_c$ and the maximum discrepancy is less than 10%. Further improvement of modeling the angles requires numerical functions, which will not be addressed herein.

The z-coordinate of the middle point equals the intercept of the elliptical function determined from (8) and (9)

$$Z_{0Hy(i)} = b_{\text{core\_}i}. \tag{11}$$

In order to solve the three unknowns α_i, β_i, and γ_i in (7) and the z-coordinate of the endpoint $Z_{c(i)}$, following four conditions are employed.

1) Point P_1 $(R_{0Hy}, Z_{0Hy(i)})$ is on the contour

$$Z_{0Hy(i)} = \gamma_i \cdot \tanh(\alpha_i \cdot (\beta_i - R_{0Hy})). \tag{12}$$

2) The tangential angle at point $P_1(R_{0Hy}, Z_{0Hy(i)})$ is 0°

$$-\alpha_i \gamma_i \cdot \{1 - \tanh^2[\alpha_i \cdot (\beta_i - R_{0Hy})]\} = 0. \tag{13}$$

3) The boundary point $P_2(R_c, Z_{c(i)})$ is on the contour

$$Z_{c(i)} = \gamma_i \cdot \tanh(\alpha_i \cdot (\beta_i - R_c)). \tag{14}$$

4) The tangential angle at point $P_2(R_c, Z_{c(i)})$ is noted as θ_c, where θ_c along the right edge of the core plate is obtained from the boundary conditions of the contour angles θ_f (see Fig. 6) in the fringing area

$$\tan\theta_{c_i} = \mu_r \tan\theta_{f\_i}(Z_{c(i)}) = -\alpha_i \gamma_i \cdot \{1 - \tanh^2[\alpha_i \cdot (\beta_i - R_c)]\}. \tag{15}$$

By solving (8)–(15) simultaneously, the flux lines in the core plate can be determined uniquely with the selected point $(R_{x(i)}, Z_p)$. Note that the flux does not necessarily span the entire range of the core, and some flux end at the upper (lower) edge of the top (bottom) core plate.

C. Winding Region

The flux contours in the winding region are approximated to be arcs with the general function

$$f_{w\_i}(r,z):\ (r-h_{\text{wind\_}i})^2+z^2=R_{\text{wind\_}i}^2 \tag{16}$$

where $h_{\text{wind\_}i}$ and $R_{\text{wind\_}i}$ are unknowns for ith contour.

With a given value of $R_{x(i)}$, the two unknowns $h_{\text{wind\_}i}$ and $R_{\text{wind\_}i}$ in (16) are determined from the conditions that point $(R_{x(i)}, Z_p)$ is on the arc and the tangential angle θ_w at point $(R_{x(i)}, Z_p)$ satisfies boundary condition with θ_p (see Fig. 8)

$$(R_{x(i)}-h_{\text{wind\_}i})^2+Z_p^2=R_{\text{wind\_}i}^2 \tag{17}$$

$$\tan\theta_{w\_i}=\frac{-(R_{x(i)}-h_{\text{wind\_}i})}{Z_p}=\mu_r\tan\theta_p(R_{x(i)}). \tag{18}$$

A complete contour can be constructed using Figs. 6 and 8, and (8)–(18) with the specified starting point $(R_{x(i)}, Z_p)$.

III. Reluctance Calculation

The reluctance of each path is the key parameter to determine the flux Φ flowing in each path. The ith path is formed by two closed contours (ith and $(i+1)$th) with starting points $(R_{x(i)}, Z_p)$ and $(R_{x(i+1)}, Z_p)$ as illustrated by the highlighted area in Fig. 4. The reluctance of each path is determined following the same method discussed in this section. It will be used in the procedure to build complete flux lines in Section IV.

The total reluctance of one path is the sum of all the reluctances in each region

$$\Re_{\text{path\_}i}=\Re_{\text{wind\_}i}+2\Re_{\text{core\_}i}+\Re_{\text{fring\_}i} \tag{19}$$

where $\Re_{\text{path\_}i}$ comprises four reluctances in series: reluctance $\Re_{\text{wind}}$ of the winding region, two equal reluctances $\Re_{\text{core}}$ of the core region, and reluctance $\Re_{\text{fringe}}$ in the fringing region [see Fig. 1(b)].

The reluctance in each region is divided into N_{inc} incremental reluctances in series, where N_{inc} is an integer. Each incremental reluctance is calculated from the equivalent area and length formed by four points $M_{i\_j}(r_{i\_j}, z_{i\_j})$, $M_{i\_j+1}(r_{i\_j+1}, z_{i\_j+1})$, $M_{i+1\_j}(r_{i+1\_j}, z_{i+1\_j})$, and $M_{i+1\_j+1}(r_{i+1\_j+1}, z_{i+1\_j+1})$ as shown in Fig. 4, where i is the index for the contour number and j is the index of point number ($1 \le j \le N_{\text{inc}}+1$).

A. Reluctance in the Winding Region

The cross sectional area through a given point $M_{i\_j}(r_{i\_j}, z_{i\_j})$ on the ith contour is calculated by finding its corresponding point $M_{i+1\_j}(r_{i+1\_j}, z_{i+1\_j})$ on the $(i+1)$th contour. The coordinates of M_{i+1_j} are determined from which they satisfy $f_{w\_i+1(r,z)}$ defined in (16)

$$(r_{i+1\_j}-h_{\text{wind\_}i+1})^2+z_{i+1\_j}^2=R_{\text{wind\_}i+1}^2 \tag{20}$$

and that the coordinates of M_{i+1_j} also satisfy the following equation such that $M_{i\_j}M_{i+1\_j}$ is perpendicular to the tangential line (derivative of $f_{w\_i+1(r,z)}$) at M_{i+1_j}:

$$-\frac{r_{i\_j}-r_{i+1\_j}}{z_{i\_j}-z_{i+1\_j}}=\frac{h_{\text{wind\_}i+1}-r_{i+1\_j}}{z_{i+1\_j}}. \tag{21}$$

The values of (r_{i+1_j}, z_{i+1_j}) can be exclusively determined from (20) and (21) for any point M_{i_j} along the ith contour, and the cross section area A_{inc} for an incremental reluctance at that point M_{i_j} is

$$A_{\text{inc}}(i,j)=\sqrt{(r_{i\_j}-r_{i+1\_j})^2+(z_{i\_j}-z_{i+1\_j})^2}\cdot\pi(r_{i\_j}+r_{i+1\_j}). \tag{22}$$

An incremental magnetic length is defined as the distance between the cross-sectional areas at $M_{i\_j}(r_{i\_j}, z_{i\_j})$ and $M_{i\_j+1}(r_{i\_j+1}, z_{i\_j+1})$, where M_{i_j+1} is an incremental point along the ith contour. The corresponding points determined from (20) and (21) on the $(i+1)$th contour are $M_{i+1\_j}(r_{i+1\_j}, z_{i+1\_j})$ and $M_{i+1\_j+1}(r_{i+1\_j+1}, z_{i+1\_j+1})$, respectively. The incremental magnetic length is calculated by connecting the midpoint of $M_{i\_j}M_{i+1\_j}$ and $M_{i\_j+1}M_{i+1\_j+1}$

$$l_{\text{inc}}(i,j)=\frac{1}{2}\sqrt{\begin{matrix}(r_{i\_j}+r_{i+1\_j}-r_{i\_j+1}-r_{i+1\_j+1})^2\\+(z_{i\_j}+z_{i+1\_j}-z_{i\_j+1}-z_{i+1\_j+1})^2.\end{matrix}} \tag{23}$$

Therefore, the incremental reluctance formed by the four points is found from the incremental magnetic length and the average cross-sectional area by

$$\Re_{\text{wind\_inc}}(i,j)=\frac{l_{\text{inc}}(i,j)}{\mu_0\frac{1}{2}(A_{\text{inc}}(i,j)+A_{\text{inc}}(i,j+1))}. \tag{24}$$

The reluctance in the winding region for ith path is found from the sum of all the incremental reluctances

$$\Re_{\text{wind\_}i}=\sum_{j=1}^{N_{\text{inc}}}\Re_{\text{wind\_inc}}(i,j) \tag{25}$$

where N_{inc} is the number of increment reluctances along the contour.

B. Reluctance in the Core Region

The incremental reluctance in the core region is found in a similar way as in the winding region, except that the equations for finding the coordinates of M_{i+1_j}, which can be expressed as

$$\frac{(r_{i+1\_j}-R_{0Hy})^2}{a_{\text{core\_}i+1}^2}+\frac{z_{i+1\_j}^2}{b_{\text{core\_}i+1}^2}=1 \tag{26}$$

$$-\frac{r_{i\_j}-r_{i+1\_j}}{z_{i\_j}-z_{i+1\_j}}=\frac{R_{0H_y}-r_{i+1\_j}}{z_{i+1\_j}}\cdot\frac{b_{\text{core\_}i+1}^2}{a_{\text{core\_}i+1}^2}. \tag{27}$$

The coordinate of $M_{i+1\_j}(r_{i+1\_j}, z_{i+1\_j})$ on the $(i+1)$th contour can be exclusively determined from (26) and (27). The cross-sectional area at each point $M_{i\_j}(r_{i\_j}, z_{i\_j})$ is given by (22) and the incremental magnetic length is given by (23), from which the incremental reluctance in the core $R_{\text{core\_inc}}(i,j)$ can be found by (24) substituting μ_0 with $\mu_0\mu_r$.

The reluctance in the core region for ith path is found from the sum of all the incremental reluctances

$$\Re_{\text{core\_}i}=\sum_{j=1}^{N_{\text{inc}}}\Re_{\text{core\_inc}}(i,j). \tag{28}$$

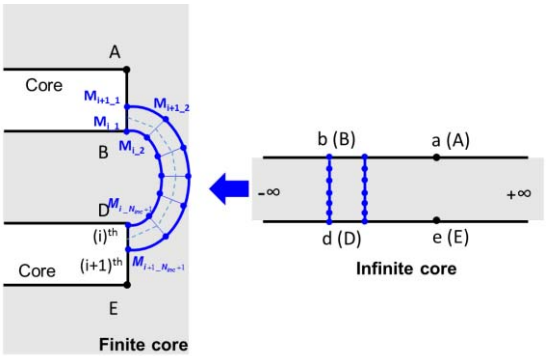

Fig. 9. Reluctance calculation in the fringing region between ith and (i+1)th contours showing the cross-sectional areas and incremental magnetic length.

TABLE I
EXAMPLE DIMENSIONS OF A PLATE-CORE INDUCTOR

Parameter	Value
R_c	5 mm
μ	80
R_{wi}	3 mm
Space	76 μm
Number of turns	16

Parameter	Value
H_c	0.3 mm
l_g	0.25 mm
R_{wo}	4.95 mm
Number of layers	2
Winding width	177 μm

C. Reluctance in the Fringing Region

The coordinates of the four points comprising the incremental reluctance are directly obtained from the transformation of the corresponding points along two vertical lines in the infinite-core domain as illustrated in Fig. 9.

The cross-sectional area at each point $M_{i\_j}(r_{i\_j}, z_{i\_j})$ is given by (22) and the incremental magnetic length is given by (23), from which the incremental reluctance in the fringing $\Re_{\text{fring\_inc}}(i, j)$ can be found by (24).

The reluctance in the fringing region for ith path is

$$\Re_{\text{fring\_}i} = \sum_{j=1}^{N_{\text{inc}}} \Re_{\text{fring\_inc}}(i, j). \tag{29}$$

IV. COMPLETE FLUX LINES

The procedure to obtain the complete flux lines is demonstrated in Fig. 10. Each flux line is obtained following the method in Section II, and each path-reluctance is calculated following the method in Section III. An "initialized" path ($i = 1$) is specified first by drawing two initialized contours starting from $(R_{x(1)}, Z_p)$ and $(R_{x(2)}, Z_p)$ as shown in Fig. 4 by highlighted area. The reluctance $R_{\text{path\_1}}$ is calculated to obtain the flux Φ based on (3). The starting points $(R_{x(i)}, Z_p)$ of the other flux lines are numerically searched such that each path carries the same Φ, successively.

The starting points of the first two contours decide the width of the initialized path and the value of the constant Φ. The dimensions of a plate-core inductor are given in Table I as an example. The point $R_{x(1)}$ is selected to be the same as R_{wi}, and the point $R_{x(2)}$ is swept from 0.85 to 0.95R_{wi}. The distance ΔR between $R_{x(1)}$ and $R_{x(2)}$ is given by $R_{x(1)} - R_{x(2)}$.

The relationships among the total number of paths, flux in each path, and ΔR are shown in Fig. 11 with 1 A excitation

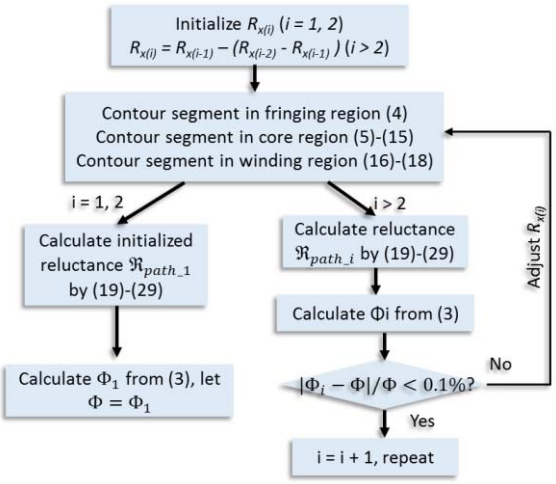

Fig. 10. Flow chart to obtain the complete flux lines for plate-core inductors.

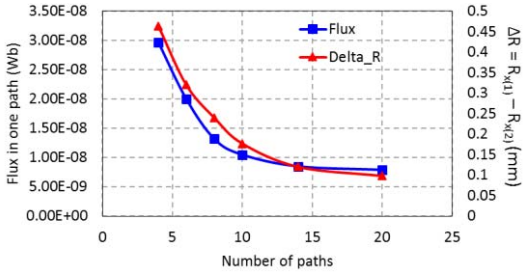

Fig. 11. Plot of flux carried by one path versus the total number of paths for structure with dimensions in Table I and 1 A current excitation.

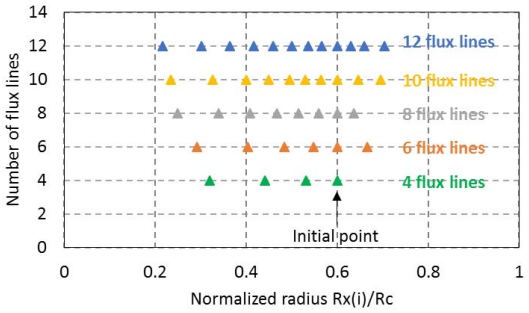

Fig. 12. Plot of starting point Rx(i) normalized to core radius Rc for different total number of flux lines with structure dimensions in Table I.

in each turn. Smaller distance between the two points leads to lower flux in each path, and more paths can be constructed within the area. The normalized radius of the starting point $R_{x(i)}$ for each flux line versus different total number of paths is shown in Fig. 12.

The modeled flux lines following the procedure in Fig. 10 are shown in Fig. 13(a) for the inductor described in Table I. The shapes of the modeled flux lines are very close to those from the simulation, which validates the modeling functions discussed in Section II.

V. MODELING RESULTS OF MAGNETIC FIELD

The flux lines shown in Fig. 13(a) are used to find the magnetic field versus space from (2). For example, the mod-

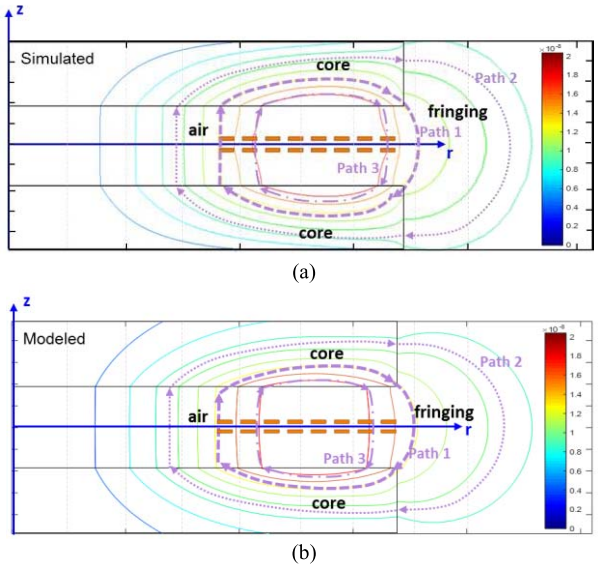

Fig. 13. Comparison of (a) simulated flux lines and (b) flux lines constructed based on proportional reluctance, equal-flux model under same scale for the plate-core inductor with dimensions listed in Table I.

eled and simulated flux density along the dashed curves in Fig 13 (a) and (b) are compared in Fig. 14. The discrepancy between model and simulation is caused by the shape approximations and crowding effect due to the presence of windings. The average error of the three paths shown is 11.4%.

The field is further verified by comparing the energy distributions. The energies stored at different regions are extracted from FES. They are compared to the corresponding energy from the model by integrating $(B^2/2\mu)$ over the volume as shown in Fig. 15. The difference of distribution percentage between the modeled and simulated energy is less than 3%.

It should be noted that the number of paths is not a major concern that impacts the model accuracy. Although larger number of paths gives better resolution of the field, the energy (inductance) integrated from the field remains constant after the number of paths is larger than 10.

VI. Experimental Verification

Magnetic field modeling allows predication of key performance factors. The inductance can be calculated from energy storage; the ac winding loss can be calculated from boundary fields near the winding [24]; and the core loss can be calculated from field distribution inside the magnetic material [25]. In this paper, only inductance is used as an index to evaluate the accuracy of the model, whereas the other factors will be reported in the future.

The inductance is calculated from the total energy divided by the square of the current. The energy stored by all the paths is found from the integration of magnetic flux density

$$L = \frac{2E}{I^2} = \frac{1}{I^2}\int \frac{B(r,z)^2}{\mu}\cdot dV. \tag{30}$$

In order to verify the inductance calculation, several winding layouts are designed and fabricated for measurement. The prototype shown in Fig. 16 consists of a 3 × 4 inductor matrix

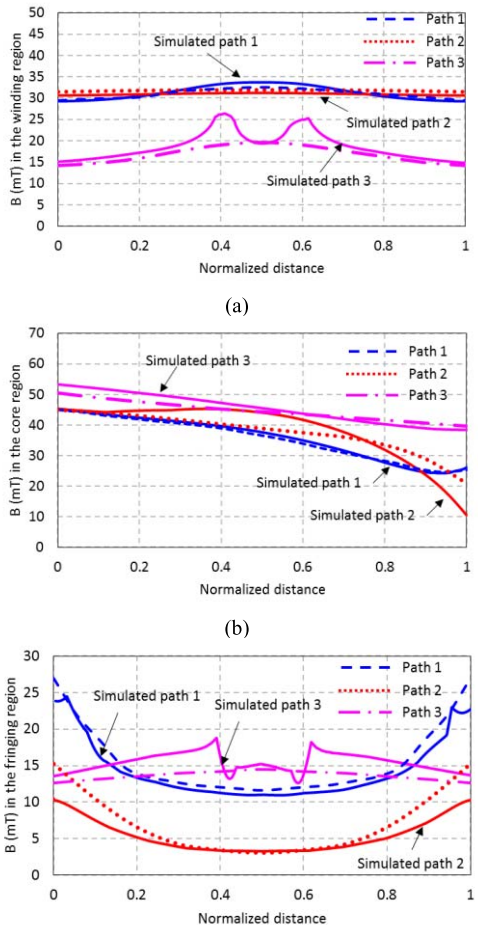

Fig. 14. Comparison of magnetic flux density along the path shown in Fig. 13. (a) Winding region. (b) Core region. (c) Fringing region.

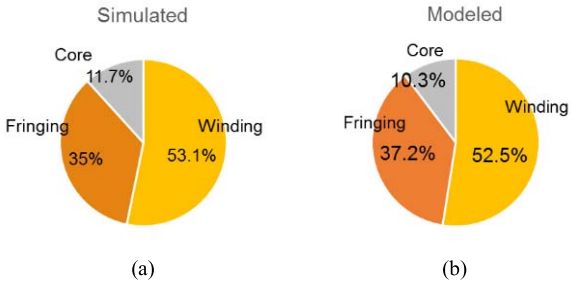

Fig. 15. Comparison of energy breakdown between (a) simulation and (b) PREF model for the plate-core inductor with dimensions listed in Table I.

with different air gap lengths, inner winding radii, and number of turns. Each row varies one parameter while keeping the other parameters at the nominal values listed in Table I. The detailed dimensions are listed in Table II.

The fabricated flexible circuit shown in Fig. 17(a) has 0.5 oz copper layers on both sides. The spacing between the winding turns is 3 mils, the dielectric spacing between the copper layers is 2 mils, and the total thickness of the sheet is kept at 0.25 mm as the nominal air gap. The air gap length of the first row is adjusted by adding polyimide-tape layers. The round plate-

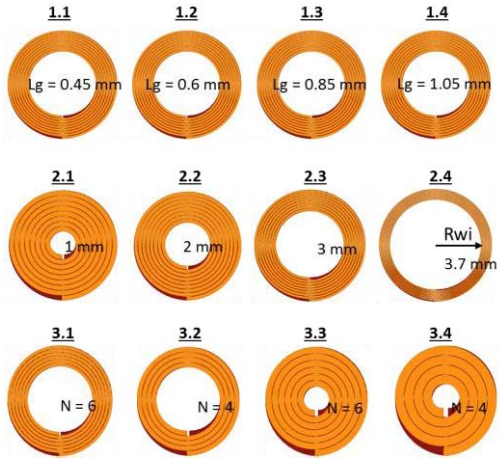

Fig. 16. Layouts of winding matrix fabricated with flexible circuit for inductance verification.

TABLE II
DIMENSIONS OF INDUCTOR PROTOTYPES

No.	R_{wi} (mm)	L_g (mm)	N/layer	W_{width} (μm)
1.1	3	0.45	8	177
1.2	3	0.6	8	177
1.3	3	0.85	8	177
1.4	3	1.05	8	177
2.1	1	0.25	8	427
2.2	2	0.25	8	302
2.3	3	0.25	8	177
2.4	3.7	0.25	8	90
3.1	3	0.25	6	262
3.2	3	0.25	4	430
3.3	2	0.25	6	428
3.4	2	0.25	4	680
R_c = 5 mm, H_c = 0.3 mm, turn-turn spacing = 3 mils, R_{wo} = 4.95 mm, winding layer spacing = 2 mils, winding thickness = 18 μm, $\mu = 80\mu_0$.				

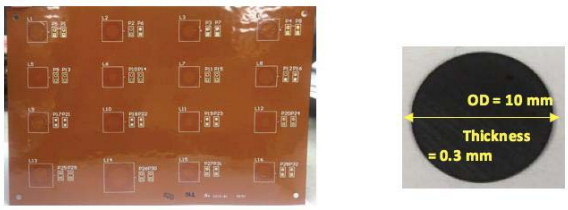

(a) (b)

Fig. 17. (a) Flexible circuit fabricated with winding layouts shown in Fig. 16. (b) Round magnetic core made of 4F1 NiZn ferrite with 10-mm diameter and 0.3-mm thickness.

core shown in Fig. 17(b) is made of 4F1 [23] material and has a diameter of 10 mm and thickness of 0.3 mm. Two fixtures are attached to the top and bottom of the flexible circuit in order to maintain a stable air gap length between the two core plates. The round core plates are inserted into the cavities on the fixtures, and the assembled prototype used for testing is shown in Fig. 18.

The prototype with inductor matrix is measured by Impedance Analyzer 4294a from Agilent with four terminals arranged in a Kelvin connection. The inductance of each layout is measured and compared to the FES and PREF models as shown in Fig. 19. For the parameters tested, the measurement

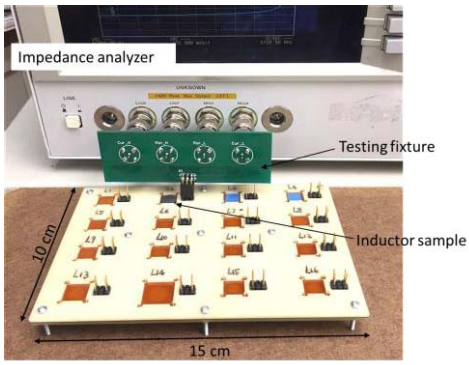

Fig. 18. Assembled inductor matrix prototype with single winding sandwiched between two fixtures on the top and bottom for stability.

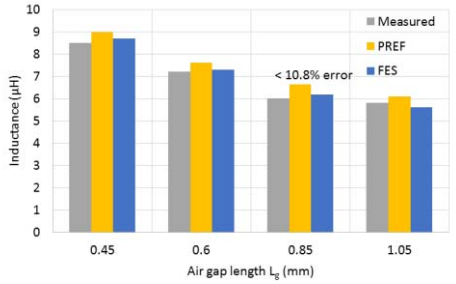

(a)

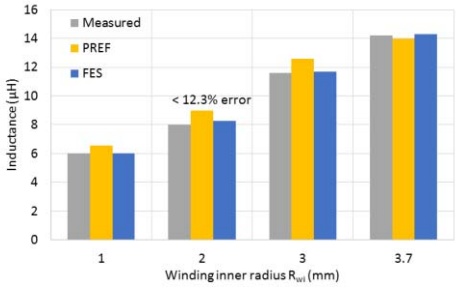

(b)

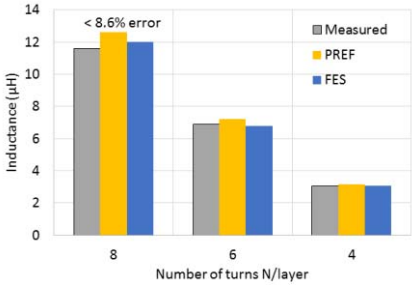

(c)

Fig. 19. Comparisons of inductance measured with FEA and PREF modeled results under different (a) air gap lengths, (b) winding inner radii, and (c) number of turns.

shows good agreement with the simulation and modeling results, with less than 16% variance.

Developing precise model gives more insights of the problem such that it is useful for design and optimization. Furthermore, the PREF model introduced herein is more computational efficient than the FES result. Taking the structure in Table I as an example, a 2-D magnetostatic simulation takes about 3 mins with adaptive mesh refinement to 1% error criterion, whereas the PREF model in MATLAB only takes 4 s

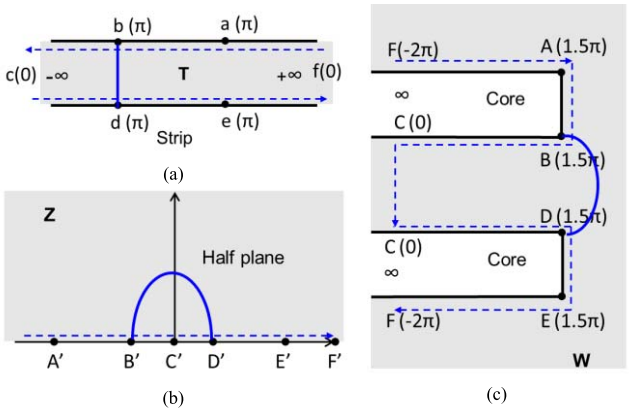

Fig. 20. Schwartz-Christoffel transformation showing one vertical contour in (a) strip domain, (b) half-plane domain, and (c) physical domain.

TABLE III
SCHWARTZ-CHRISTOFFEL TRANSFORMATION

Vertices	W	Z	T	$\alpha_w(\pi)$	$\alpha_T(\pi)$
A	$R_c+(H_c+0.5l_g)\cdot j$	-1	T_E+j	1.5	1
B	$R_c+0.5l_g\cdot j$	$-Z_D$	$0+j$	1.5	1
C	∞	0	$-\infty$	0	0
D	$R_c-0.5l_g\cdot j$	Z_D	0	1.5	1
E	$R_c-(H_c+0.5l_g)\cdot j$	1	T_E	1.5	1
F	∞	∞	∞	-2	0

Values of Z_D and T_E vary with H_c and l_g that can be determined numerically by Matlab SC-toolbox.

to generate the field for inductance calculation. The difference would be more dramatic for complex structures with more number of turns or larger winding dimensions than the skin depth.

VII. CONCLUSION

The PREF model is introduced to model the magnetic field distribution for the plate-core inductors with finite core dimension ($R_{wo} \approx R_c$). The PREF model is motivated by generating equal-flux lines by making the reluctance of each path proportional to the Ampere-turns. Two elliptical functions, a hyperbolic tangent function, and SC transformations are used to model the shape of the flux lines guided by FES. The procedure to construct all the flux lines is demonstrated with an example, and the number of total flux lines is governed by the selection of the initial path. The magnetic field at an arbitrary position can be found from these equal-flux paths. The inductance (energy) based on the field modeled is verified by both FES and experimental results. Compared to existing modeling method, the error for field calculation is reduced to <10% by considering the fringing behavior with a finite core dimension. The application of this method to coupled inductors, as well as ac losses calculation based on the field, will be covered in future publications.

APPENDIX A

The SC theorem states that the interior points of a strip or a polygon bounded by straight lines can both be transformed into points in the upper-half-plane. The equation that represents this transformation is

$$\frac{dW}{dZ} = k_1 \cdot \prod_{j=1}^{n} (z - z_j)^{\alpha_{wj}-1} \tag{31}$$

$$\frac{dT}{dZ} = k_2 \cdot \prod_{j=1}^{n} (z - z_j)^{\alpha_{Tj}-1} \tag{32}$$

where T is the strip domain; Z is the upper-half-plane domain; W is the physical domain; z_j are the corresponding images of the vertices in physical domain; α_{Tj} and α_{wj} are the interior angles of the vertices in T and W domains, respectively; n is the total number of vertices; k_1 and k_2 are constants.

In the first step, the two core plates are treated as a polygon with vertices *ABCDEF* [see Fig. 20(a)], where C and F end at infinity. This polygon in W domain is mapped to Z domain with corresponding points $A'B'C'D'E'F'$ from left to right on the real axis [see Fig. 20(b)]. The point C' is selected to be 0 as it serves as the symmetric point in Z domain; the two points farther from the air gap A and E are mapped to -1 and 1 in the Z domain; points B and D are mapped to $-Z_D$ and Z_D where Z_D is a value determined from numerical solutions; and F is mapped to infinity. In the second step, a strip with vertices *abcdef* [see Fig. 20(c)] can be found that mapped to the same points on the Z domain. Points c and f are infinities to the negative and positive side; points b and d are selected to be $(0+j)$ and 0; points a and e are found from numerical solutions with values (T_E+j) and T_E, respectively. Therefore, any vertical line within the T domain becomes a flux line in the fringing area of the W domain as demonstrated in Fig. 20. Table III summarizes the vertices and angles in each domain.

MATLAB provides a toolbox that provides SC transformation among strip domain, physical domain, and upper-half-plane based on numerical solutions so that the value of Z_D and T_E can be determined.

The mapping function from Z to W is the integral of (31)

$$W = k_1 \int \prod_{j\equiv A \text{ to } F} (z - z_j)^{\alpha_{wj}-1} dz + C_1$$

$$= k_1 \int \frac{\sqrt{z^2-1}\cdot\sqrt{z^2-Z_D^2}}{z} dz + C_1. \tag{33}$$

Substitute z^2 in (33) by x and the indefinite integral of x becomes

$$W = k_1 \int \frac{\sqrt{x-1}\cdot\sqrt{x-Z_D^2}}{x} dx + C_1 = k_1 \cdot f(x) + C_1 \tag{34}$$

where

$$f(x) = \sqrt{x-1}\cdot\sqrt{x-Z_D^2} - a_1 \cdot \operatorname{arcsinh}(a_2 \cdot \sqrt{x-1})$$
$$+ a_3 \ln(a_4 - a_5\sqrt{x-1}\cdot\sqrt{x-Z_D^2} - a_1 x)$$
$$- a_3 \ln(a_4 + a_5\sqrt{x-1}\cdot\sqrt{x-Z_D^2} - a_1 x)$$

$$C_1 = R_c - (H_c + 0.5l_g) \cdot j$$
$$k_1 = \frac{R_c - 0.5l_g \cdot j - C_1}{f(x = Z_D^2)} \tag{35}$$

where $x = z^2$, a_1, a_2, a_3, a_4, and a_5 are constants dependent on Z_D.

The transformation function from T to Z is the integral of (32)

$$T = k_2 \int \prod_{j \equiv A \text{ to } F} (z - z_j)^{\alpha_{Tj}-1} dz + C_2 = k_2 \ln(z) + C_2 \tag{36}$$

where C_2 and k_2 are constants determined from the value of T_E and Z_D

$$C_2 = T_E$$
$$k_2 = \frac{-C_2}{\ln(z_D)}. \tag{37}$$

APPENDIX B

The parameter R_{0Hy} is the position along the r axis where the vertical magnetic field H_y becomes zero. The flux flows from bottom to top core plate (assuming current direction points into the page) when $0 < r < R_{0Hy}$, and flows from top to bottom core plates for $r > R_{0Hy}$. The amount of flux from R_{wi} to R_{0Hy} is equal to that from R_{0Hy} to R_c

$$\Phi_{R_{\text{wi}}\_R_{0Hy}} = \Phi_{R_{0\text{Hy}}\_R_c}. \tag{38}$$

Therefore, the amount of flux from 0 to R_{0Hy} is one half of the sum of flux from 0 to R_{wi} and 0 to R_c:

$$\Phi_{R_c} + \Phi_{R_{\text{wi}}} = \Phi_{R_{\text{wi}}} + 2\Phi_{R_{\text{wi}}\_R_{0Hy}} + \Phi_{R_{\text{wi}}} = 2\Phi_{R_{0Hy}}$$
$$\Phi_{R_{0Hy}} = \frac{1}{2}(\Phi_{R_c} + \Phi_{R_{\text{wi}}}). \tag{39}$$

The flux has the same relationship as the permeance, so the position of the R_{0Hy} is found from

$$\frac{\mu_0 \pi R_{0Hy}^2}{l_g} = \frac{1}{2}\left(\frac{\mu_0 \pi R_{\text{wi}}^2}{l_g} + \frac{\mu_0 \pi R_c^2}{l_g}\right)$$
$$R_{0Hy} = \sqrt{\frac{1}{2}\left(R_{\text{wi}}^2 + R_c^2\right)}. \tag{40}$$

REFERENCES

[1] M. Kazimierczuk, *High-Frequency Magnetic Components*, 2nd ed. New York, NY, USA: Wiley, 2014, pp. 9–26, pp. 163–381.

[2] Q. Li, D. Yan, and F. C. Lee, "High density low profile coupled inductor design for integrated Point-of-Load converter," in *Proc. 25th Annu. IEEE Appl. Power Electron. Conf. Expo*, Feb. 2010, pp. 79–85.

[3] Z. Ouyang and M. A. E. Andersen, "Overview of planar magnetic technology—Fundamental properties," *IEEE Trans. Power Electron.*, vol. 29, no. 9, pp. 4888–4900, Sep. 2014.

[4] C. Quinn, K. Rinne, T. O'Donnell, M. Duffy, and C. O. Mathuna, "A review of planar magnetic techniques and technologies," in *Proc. IEEE Appl. Power Electron. Conf. Expo*, vol. 2. Mar. 2001, pp. 1175–1183.

[5] Z. Ouyang, O. C. Thomsen, and M. A. E. Andersen, "Optimal design and tradeoff analysis of planar transformer in high-power DC–DC converters," *IEEE Trans. Ind. Electron.*, vol. 59, no. 7, pp. 2800–2810, Jul. 2012.

[6] Y. P. Su, X. Liu, and S. Y. R. Hui, "Mutual inductance calculation of movable planar coils on parallel surfaces," *IEEE Trans. Power Electron.*, vol. 24, no. 4, pp. 1115–1123, Apr. 2009.

[7] Y. P. Su, X. Liu, and S. Y. Hui, "Extended theory on the inductance calculation of planar spiral windings including the effect of double-layer electromagnetic shield," *IEEE Trans. Power Electron.*, vol. 23, no. 4, pp. 2052–2061, Jul. 2008.

[8] T. Inoue, K. Nishijima, S. Yatabe, T. Mizoguchi, and T. Sato, "The effect of magnetic film structure on the inductance of a planar inductor," *IEEE Trans. Magn.*, vol. 34, no. 4, pp. 1372–1374, Jul. 1998.

[9] A. Balakrishnan, W. D. Palmer, W. T. Joines, and T. G. Wilson, "The inductance of planar structures," in *Proc. IEEE Appl. Power Electron. Conf. Expo*, Mar. 1993, pp. 912–921.

[10] E. Waffenschmidt, B. Ackermann, and J. A. Ferreira, "Design method and material technologies for passives in printed circuit board embedded circuits," *IEEE Trans. Power Electron.*, vol. 20, no. 3, pp. 576–584, May 2005.

[11] A. Bouabana and C. Sourkounis, "Design and analysis of a coreless flyback converter with a planar printed-circuit-board transformer," in *Proc. 12th Int. Conf. Optim. Elect. Electron. Equip. (OPTIM)*, May 2010, pp. 557–563.

[12] K. D. T. Ngo, E. Alpizar, and J. K. Watson, "Modeling of losses in a sandwiched-winding matrix transformer," *IEEE Trans. Power Electron.*, vol. 10, no. 4, pp. 427–434, Jul. 1995.

[13] E. Waffenschmidt, "Homogeneous magnetic coupling for free positioning in an inductive wireless power system," *IEEE J. Emerg. Sel. Topics Power Electron.*, vol. 3, no. 1, pp. 226–233, Mar. 2015.

[14] W. A. Roshen, "Analysis of planar sandwich inductors by current images," *IEEE Trans. Magn.*, vol. 26, no. 5, pp. 2880–2887, Sep. 1990.

[15] W. G. Hurley and M. C. Duffy, "Calculation of self- and mutual impedances in planar sandwich inductors," *IEEE Trans. Magn.*, vol. 33, no. 3, pp. 2282–2290, May 1997.

[16] R. Jones, "Analysis of the efficiency and inductance of multiturn thin film magnetic recording head," *IEEE Trans. Magn.*, vol. 14, no. 5, pp. 509–511, Sep. 1978.

[17] T. Sato, T. Mizoguchi, and M. Sahashi, "Simulation of micro magnetic devices," *IEEE Transl. J. Magn. Jpn.*, vol. 9, no. 4, pp. 68–75, Jul. 1994.

[18] M. Lu, K. D. T. Ngo, M. Filippa, and W. Bicknell, "Model for electromagnetic actuator with significant fringing using minimal fitting parameters," *IEEE Trans. Magn.*, vol. 51, no. 1, Jan. 2015, Art. no. 8000207.

[19] C. Chillet and J. Y. Voyant, "Design-oriented analytical study of a linear electromagnetic actuator by means of a reluctance network," *IEEE Trans. Magn.*, vol. 37, no. 4, pp. 3004–3011, Jul. 2001.

[20] A. Balakrishnan, W. T. Joines, and T. G. Wilson, "Air-gap reluctance and inductance calculations for magnetic circuits using a Schwarz-Christoffel transformation," *IEEE Trans. Power Electron.*, vol. 12, no. 4, pp. 654–663, Jul. 1997.

[21] M. Markovic, M. Jufer, and Y. Perriard, "Analyzing an electromechanical actuator by Schwarz-Christoffel mapping," *IEEE Trans. Magn.*, vol. 40, no. 4, pp. 1858–1863, Jul. 2004.

[22] *Schwarz-Christoffel Toolbox User's Guide*, accessed on Mar. 2017. [Online]. Available: http://www.math.udel.edu/~driscoll/SC/guide.pdf

[23] *Ferroxcube 4F1 NiZn Material Datasheet*, accessed on Mar. 2017. [Online]. Available: http://www.ferroxcube.com/FerroxcubeCorporateReception/datasheet/4f1.pdf

[24] N. Wang, T. O'Donnell, and C. O'Mathuna, "An improved calculation of copper losses in integrated power inductors on silicon," *IEEE Trans. Power Electron.*, vol. 28, no. 8, pp. 3641–3647, Aug. 2013.

[25] D. Lin, P. Zhou, W. N. Fu, Z. Badics, and Z. J. Cendes, "A dynamic core loss model for soft ferromagnetic and power ferrite materials in transient finite element analysis," *IEEE Trans. Magn.*, vol. 40, no. 2, pp. 1318–1321, Mar. 2004.